A Non-Destructive Testing Method in Industrial Processes to Determine the Complex Refractive Index Using Ultra-Wide Band Radio

Vipin Choudhary, *Member, IEEE*, Patrik Ottosson, Daniel Andersson, and Daniel Rönnow, *Member, IEEE*

***Abstract*—An ultra-wide band measurement method for determining the complex refractive index of large-volume objects is presented. The method is intended for industrial non-destructive testing. It uses a frequency-domain technique in which transmitted radio pulses are analyzed and the effects of near field and coupling on the determined refractive index are compensated. Measurements were performed in an industrial setup with electromagnetic sensors buried in the object. The results are presented for woodchips as an object. The refractive index was experimentally determined in the frequency range 0.5-3.0 GHz. Additionally, we designed and manufactured planar quasi-differential elliptical-antennas as electromagnetic sensors. The results from the industrial measurement setup were compared with the results of the laboratory setup, in which the sensors were placed outside the test box and near field and coupling effects could be neglected. The complex refractive index determined for the two setups was in good agreement, which corroborates the proposed method for compensating for coupling and near-field effects. The complex refractive index of woodchips changes with the moisture content. It is experimental verified using the industrial setup that the moisture content can be determined with a 2 percent error.**

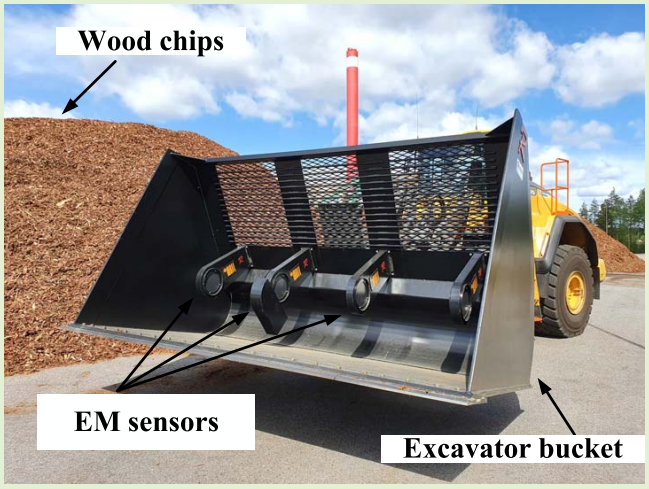

***Index Terms*—Complex refractive index, non-destructive testing, UWB radar sensor, moisture, wood-based material, radio-link system, EM sensor, woodchips, near field coupling, radio measurement.**

I. Introduction

ULTRA-WIDE band (UWB) radar systems are used in various short range applications [1],[2]. Free space non-destructive testing using radar system is suitable for quick measurements of large volume objects [3], [4]. Determining the accurate complex refractive index of large volume objects is of great importance in trading (grain, soil, sand, wood and wood-based material), sorting, and in industrial processing [5], especially during the open storage of materials such as grain, soil and wood, which can absorb water content from 1% to 200 % depending on pressure, temperature, humidity in air, and surface air [4], [5].

Woodchips are used in the pulp and paper industry, and its moisture content is a quality parameter [6]. When used in district heating plants, the moisture content of woodchips affects the CO_2 emissions and the efficiency of combustion [7], [8]. Moreover, woodchips are used also to fuel updraft gasifiers to produce syngas (synthesis gas), wherein the moisture content affects the production of CO, H_2, and CH_4, [9].

In the literature, several non-destructive testing techniques using radar and radio-link systems have been reported, in which sensors were either buried/submerged in substances or inside objects or placed at a distance from objects. In [10], a near-field non-destructive testing technique for limestone was presented, in which the radar system was placed close to the limestone to monitor the real and imaginary parts of the permittivity of dry and saturated layers of a limestone-slab. Similarly, free space measurement methods for determining

Manuscript received January 20, 2022; accepted February 19, 2022. Date of publication March 2, 2022; date of current version April 14, 2022. The work was supported by Energimyndigheten (The Swedish Energy Agency). The associate editor coordinating the review of this article and approving it for publication was Prof. Piotr J. Samczynski. *(Corresponding author: Vipin Choudhary.)*

Vipin Choudhary and Daniel Rönnow are with the Department of Electrical Engineering, Mathematics and Science, University of Gävle, 801 76 Gävle, Sweden (e-mail: vinchy@hig.se; dalrow@hig.se).

Patrik Ottosson and Daniel Andersson are with Radarbolaget AB, 802 67 Gävle, Sweden (e-mail: patrik.ottosson@s-group.se).

Digital Object Identifier 10.1109/JSEN.2022.3155874

the complex refractive index of woodchips for industrial in-line applications were presented in [4], in which radar sensors were placed in the Fresnel zone (or in a far-field region).

In [11], the permittivity of a ridge of sand was determined based on reflected-pulse characteristics using electromagnetic (EM) sensors (vertically placed over the different objects). The ability of radar echoes to penetrate dielectric materials (with moderate attenuation) has been harnessed to monitor steam-assisted gravity drainage in [12], in which several experiments were conducted using UWB sensors. Furthermore, in [12], wave characteristics, wave propagation, and calibration measurements were performed in dry and wet sand (wherein sensors were fully buried inside the sand). In [13], to inspect the moisture content and the quality of concrete blocks, an electromagnetic sensor (EM sensor) was buried inside the concrete, and the correlation between scattering parameter's (S_{11} or S-parameter) amplitude and moisture content was observed. Further, the effect of soil-water content on the buried EM sensor was presented in [14], in which the experimental results showed that burying the EM sensor causes a shift in the operating frequencies to lower frequencies and that moisture in the soil degrades the buried sensor impedance matching (i.e., introduces near-field coupling with the moist soil). Similar results were shown in [15], wherein the EM sensors were buried in snow and as a result, due to coupling the transmission band of the EM sensor shifted slightly towards lower frequencies. In [16], the EM wave propagation from buried EM sensors was studied using a time-domain technique, and a matching dielectric material was used between the sensor and ground to reduce the impedance mismatching and near-field coupling effects. Hence, we can infer that the performance of an EM sensor (i.e., sensor output) depends on the dielectric properties of the material in which the sensor is buried.

This paper presents a measurement system for determining the complex refractive index of woodchips from UWB radio measurements in the buckets of wheel loaders (or big excavator buckets) used in an industrial plant. The EM sensor design is described. It also presents a general measurement method for determining the refractive index of large volume objects. In particular, it presents a study of buried EM sensors' effect on the determination of complex refractive index (or complex permittivity). Real and imaginary parts of the refractive index are determined for a large volume of objects (on an industrial scale), which makes it fit for classification in industrial testing. In this paper, investigated objects are woodchips with different moisture percentages. The presented method provides possible measurements for larger volumes, suitable for industrial sorting applications. The measurement method could also be used for objects such as grains, sand, peat, wood-based materials, and fuels (plastic, rubber, and organic materials). The method for determining the refractive index could be used in other applications where EM sensors are submerged in the substance that is being investigated.

In this paper, we have used an M-sequence radio-link system, which is manufactured and commercially available at Radarbolaget AB, Gävle, Sweden. A block diagram of the radio-link system and the experimental geometry are shown in Fig. 1. The radio-link system — used to measure the time delay of received pulses — uses an M-sequence UWB radar technique [17], in which the transmitted signal,$u(t)$, is a binary-sequence, which is distributed over the entire measurement time. The measured response after delay and attenuation is $y(t)$. The correlated signal is calculated, $u_c(t) = u(t)^* y(-t)$,where * denotes convolution. The signal $u_c(t)$ depends on the complex refractive index of the objects, as discussed in depth in [17]. A benefit of working with the correlation signal processing technique is noise suppression. The signal post-processing incorporates a time-domain and frequency-domain analysis. Moreover, the transmittance measurements make the analysis simpler than for, e.g., reflectance measurements and complements more complex analysis as in [4], in which pulses from different interfaces were analyzed in time domain using pulse windowing. A good determination of the moisture content of the woodchips can be made by compensating for the error (due to near-field coupling) in the determination of the real and imaginary part of the refractive index. Near-field coupling correction (NFCC) is discussed in depth below. Further, the best-fit polynomial is used to model the experimental data from different order polynomials, and we determine the polynomial coefficient from the experiment data. Furthermore, the properties of the sensing system in terms of sensor characteristics are discussed.

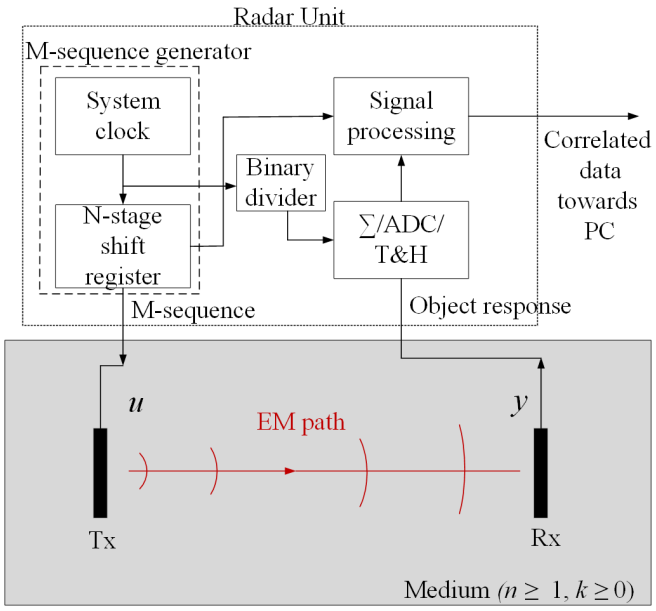

Fig. 1. The geometry of the experiment using the radio-link system (sensing system) for determining the time delay of the received pulses, showing a pair of sensor buried inside medium. Tx and Rx are the transmitting and receiving antenna. The distance between the antennas is one meter.

This paper is organized as follows: Section II describes the sensor and measurement system, which are used in industrial and laboratory measurements. The refractive index determination method, industrial system experiments, laboratory experimental verification, and NFCC results are presented in Section III; Section IV presents the discussions followed by the conclusions in Section V.

II. Sensors and System

The sensing system consists of a digital radar-processing unit (see Fig. 1) with the ability to connect one or more sensor pairs. In a pair of sensor, one antenna acts as transmitter, and the other as receiver. The system is a commercially available UWB radar system, developed by Radarbolaget AB, Sweden [18]. The system is capable of transmitting and receiving ultra-wide band signals (in the frequency range of 0.5 - 3 GHz) and is equipped with a Vivaldi antenna in the transmitter and receiver unit. The transmitting antenna emits the binary M-sequence code as a signal and the receiving antenna received the signal, which propagated through the medium or object as shown in Fig. 1. The radar unit is responsible for pre-processing of radio signals and synchronization of the transmitter and receiver unit, and generates correlated signals as output. These output signals can be presented as medium/object response in 2D time domain graph, wherein the x-axis represents the time, d/c_0, (where d is the distance between the transmitting and receiving antenna) and the y-axis represents the amplitude of the correlated signal.

Vivaldi antennas are end-fire antennas and are known to have a unidirectional focused radiation pattern of the main lobe [4], [19]. However, in the present application, bi-directional antennas were preferred in order to enable two or more channels without adding extra sensors; i.e., one transmitter can be used with two receivers. This also enables the measurement of woodchips at different places in the container. In addition, it was also preferable to have thin sensors that give minimal friction and obstruction with woodchips during the filling process. Moreover, we could not use omni-directional antennas or antennas with broad radiation patterns because power in unwanted propagation directions leads to a decrease in the signal-to-interference ratio. In addition, measurements in a close geometry may cause overlap of signals due to multi-path propagation. In this work, a reported antenna design, [20], (i.e., planar differential elliptical antenna (DEA), which shows a bi-directional radiation pattern and exhibits low-dispersion characteristics over a wide-frequency spectrum) was used as the base design. Moreover, to make the antennas capable of operating in the system's frequency range, i.e., 0.5 - 3 GHz, and to achieve linearly polarized output, the design in [20] was modified to a UWB quasi-DEA (QDEA). The linearly polarized transmit and receive characteristics of the sensors enable polarimetric measurements in the future, such a as HH, HV, VH, VV (where H denotes the horizontal and V the vertical polarization of the transmitted and received waves, respectively). Further, in this section, we describe the design and experimental results of the antenna's characterization.

A. Design

The EM sensor design and a photograph of the sensor are shown in Fig. 2. The design lies in the x-y plane. The top and bottom layers are metallic copper sheets (with a thickness of 35μm, and a conductivity of5.8×10^7S/m) attached on the dielectric layer. The Rogers RO4350B substrate ($\varepsilon_r = 3.36$, $\tan\delta = 0.0031$, with a thickness of $t = 1.6$ m) functions as a dielectric layer. On the top, there are two (symmetrical) ellipse-shaped radiating elements, whereas, at the bottom a parasitic ground is present. The feeding notch and the slot in the radiating structure (see Fig. 2 a, in which the radiating structures are highlighted in a light grey color) act as a reactive load to widen the frequency bandwidth and contribute to smaller reflection or mismatch between the 50 Ω ports and the radiating elements. The presented EM sensor was designed using an ANSYS electronics simulator [21]. We applied the optimization algorithm available in the software to optimize the design parameters. The main aim of optimization was to achieve good impedance matching to free space in the range 0.5–3.0 GHz without degrading the bi-directional radiation pattern of the EM sensor. The optimized parameters were $L_{x1} = 6$ cm,$L_{x2} = 1.4$ cm, and $L_y = 9.3$ cm . The EM sensor was excited using two identical differential feeding cables at two feeding notches of the radiating structure shown in Fig. 2. The simulated magnitude of the scattering parameter S_{11} vs. frequency is shown in Fig. 3 for the optimized EM sensor.

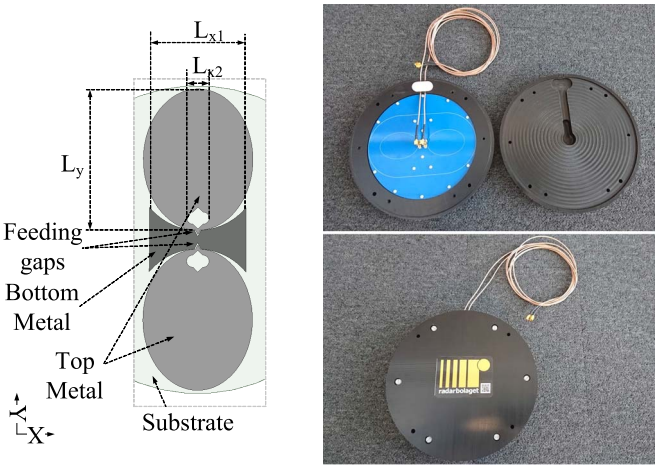

Fig. 2. (a) The design of the proposed QDEA (EM-sensor) and (b) a photograph of the sensor (in blue color) with differential feeding cables and outer plastic cover (in black color).

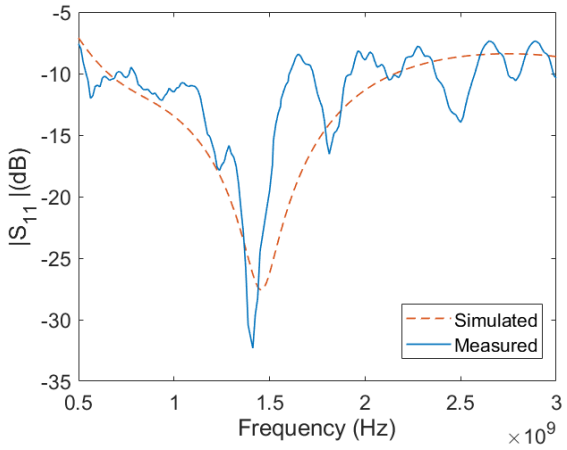

Fig. 3. Simulated (orange dashed line) and measured (blue line) magnitude of S_{11} parameter vs frequency of used EM-sensor.

B. Results

The manufacturing of the EM sensor was made by printing the antenna design on a RO4350B substrate. The SMA connectors were mounted to the antenna to which cables were attached (see Fig. 2). The antenna was placed in a milled plastic holder made of Robalon RM. This is a construction plastic made of polyethylene with low dielectric permittivity and low absorption of water.

The experimental magnitude of S_{11} of the sensor vs. frequency is shown in Fig. 3 together with the simulated results. It can be clearly seen that the experimental results of the S-parameter of the prototype sensor are consistent in magnitude below -7 dB with simulated results. However, fast variation in the magnitude of the S-parameter can be observed in the figure, which are due to imperfect matching and multiple reflections (as expected, introduced by connectors) in the measured S-parameter. Manufacturing errors and additional connector length (which increases the effective length of the feed line) are a possible reason for the slight shift of maxima and minima in the experimental data. Moreover, the sensor was capable of operating in the intended frequency spectrum, which means that it is also suitable for use in UWB systems.

EM sensor characterization was carried out by mounting the fabricated sensor inside an anechoic chamber. Initially, the S-parameters were measured using vector network analyzer (VNA-ZNB 8, Rohde & Schwarz in the frequency range 0.5– 3.5 GHz) and a manufactured antenna sensor (see Fig. 2 b). To measure the radiation pattern of the manufactured sensor, a measurement setup was prepared inside an anechoic chamber. An ultra-wideband reference horn antenna (Aaronia AG, 04518) was used as transmitting sensor while the manufactured prototype as receiving sensor. The transmitting sensor was fixed whereas the receiving sensor was rotated and the distance between the two was 1 m during EM sensor characterization [22]. The experimental radiation pattern of the proposed sensor is shown in Fig. 4. It can be seen that the sensor is bi-directional (see black color line), which is compared with the omni-directional EM sensor (see red color line). Moreover, the EM sensor did not achieve an ideal bi-directional radiation pattern due to imperfection of the sensors, partly due to the interaction with metal stands (used as supporting structure). The measurements show that the radiation pattern also carried some radiation in undesired directions (see Fig. 4). However, in this figure, it can be clearly seen that 0° and 180° have a null point while ±90° has two maxima.

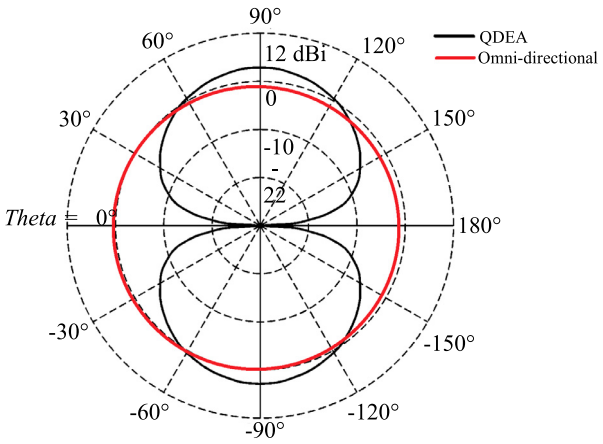

Fig. 4. Experimental radiation pattern of the used EM sensor (black line). The receiving sensor was stationary while the transmitting senor was rotated. Red line: omni-directional antennas.

III. Refractive Index Determination

The presented measurement system is intended for woodchips. Wood does not have ferro- or ferri-magnetic properties and the EM-response is linear. We assume that the woodchips can be treated as electromagnetic homogeneous linear media, which means that any heterogeneities must be on length scales much smaller than the operating wavelength of the radar system, i.e., effective medium [23] The EM interaction is then described by the complex refractive index, $\tilde{n} = n + jk$,which is related to the complex permittivity,$\tilde{\varepsilon} = \varepsilon' + j\varepsilon''$, by $\varepsilon' = n^2 - k^2$ and$\varepsilon'' = 2\,nk$. The geometry of the experiment using the radio-link transmission system is shown in Fig. 1, wherein it also illustrates the transmission of EM signals through the medium$n \geq 1$, $k \geq 0$. The radar signal,$u(t)$, is emitted by the transmitting sensor and $y(t)$is received by the receiving sensor. The distance between the sensors is$d$. The distance between the sensors is large enough such that the receiving sensor is not in the reactive near-field region, but in the Fresnel region or beyond, where the electric and magnetic fields are perpendicular, i.e.,$d > 2d_a^2/\lambda$ where d_a is the sensors' maximum dimension, and λ is the wavelength of the EM signal [24]. The method for determining the refractive index is presented in Subsection A. The model and its assumptions (see Subsection A) to determine the complex refractive index of the woodchips, were experimentally investigated in two different measurement setups (Subsection B and C). Industrial system experiments (Subsection B) are associated with real industrial non-destructive testing of woodchips, in which sensors are buried inside the woodchips during measurements. Laboratory experimental verification (Subsection C) is associated with a well-controlled test-box measurement setup in a laboratory, wherein sensors are placed outside the test box. The measured and calculated moisture content in woodchips are presented and discussed in Subsection D.

A. Method

The transmitted, and received signal are related by

$$y(t) = u(t) * h(t), \tag{1}$$

where $u(t)$ and $y(t)$ are the transmitted and received EM-signals, $h(t)$ is the impulse response, and $*$ denotes $(\tilde{n} = n + jk)\, k_{eff} n_{eff}$ convolution. We calculated the Fourier transform of the received signals. In a reference measurement, wherein $n = 1, k = 0$, the received signal is

$$Y_{ref}(\omega) = H_{ref}(\omega) U(\omega), \tag{2}$$

$$Y_{ref}(\omega) = \underbrace{S_{ref,Tx}(\omega) S_{ref,Rx}(\omega) e^{-j\omega\tau_{ref}}}_{H_{ref}(\omega)} U(\omega), \tag{3}$$

where $\tau_{ref} = d/c_0$, c_0 is the speed of light in vacuum, $U(\omega)$ is the Fourier transform of $u(t)$, etc., $S_{ref,Tx}(\omega)$ and

TABLE I
REAL AND IMAGINARY PART OF THE REFRACTIVE INDEX ($\tilde{n} = n + jk$)

n_{eff} \ k_{eff}	0.01	0.04	0.09	0.11	0.17	0.19	0.26	0.36	0.41	0.49
1.08	1.10+0.06j	1.10+0.09j	1.10+0.15j	1.10+0.19j	1.10+0.25j	1.10+0.28j	1.10+0.35j	1.10+0.39j	1.08+0.44j	1.09+0.50j
1.17	1.20+0.06j	1.20+0.09j	1.20+0.15j	1.20+0.18j	1.20+0.25j	1.20+0.28j	1.20+0.34j	1.20+0.39j	1.19+0.44j	1.18+0.50j
1.28	1.30+0.06j	1.30+0.09j	1.30+0.15j	1.30+0.18j	1.30+0.25j	1.30+0.28j	1.30+0.34j	1.30+0.39j	1.28+0.44j	1.28+0.50j
1.38	1.40+0.06j	1.40+0.09j	1.40+0.15j	1.40+0.18j	1.40+0.25j	1.40+0.28j	1.40+0.34j	1.40+0.39j	1.40+0.44j	1.39+0.50j
1.47	1.49+0.06j	1.49+0.09j	1.49+0.15j	1.49+0.18j	1.49+0.25j	1.49+0.28j	1.49+0.35j	1.49+0.39j	1.48+0.44j	1.48+0.50j
1.58	1.60+0.05j	1.60+0.08j	1.60+0.15j	1.60+0.18j	1.60+0.25j	1.60+0.28j	1.60+0.34j	1.60+0.39j	1.60+0.44j	1.59+0.50j
1.68	1.70+0.05j	1.70+0.09j	1.70+0.15j	1.70+0.18j	1.70+0.25j	1.70+0.28j	1.70+0.34j	1.70+0.39j	1.69+0.44j	1.69+0.50j
1.78	1.80+0.05j	1.80+0.08j	1.80+0.15j	1.80+0.18j	1.80+0.25j	1.80+0.28j	1.80+0.34j	1.80+0.39j	1.79+0.44j	1.79+0.50j
1.88	1.90+0.05j	1.90+0.08j	1.90+0.15j	1.90+0.18j	1.90+0.25j	1.90+0.28j	1.90+0.34j	1.90+0.39j	1.90+0.42j	1.89+0.49j
1.98	2.00+0.05j	2.00+0.08j	2.00+0.15j	2.00+0.16j	2.00+0.23j	2.00+0.26j	2.00+0.31j	2.00+0.39j	1.99+0.43j	1.98+0.49j

$S_{ref,Rx}(\omega)$ are the transmitting sensor's and receiving sensor's transfer function in air. Similarly, in an object measurement, wherein$n \neq 1, k \neq 0$, the received signal is

$$Y_{n,k}(\omega) = H_{n,k}(\omega)U(\omega), \tag{4}$$

$$Y_{n,k}(\omega) = \underbrace{S_{n,k,Tx}(\omega)S_{n,k,Rx}(\omega)e^{-j\omega\tau_{n,k}}e^{-\omega k\frac{d}{c_0}}}_{H_{n,k}(\omega)}U(\omega), \tag{5}$$

where $\tau_{n,k} = nd/c_0$, $S_{n,k,Tx}(\omega)$ and $S_{n,k,Rx}(\omega)$ are the transmitting sensor's and receiving sensor's transfer function in medium. These include the coupling between the sensor and the medium that it is submerged in. They also include the shift in frequency caused by the change in electrical length of a sensor (antenna) submerged in a medium. The received signals' dependence on the distance between transmit and receive sensors was also included in the transfer functions.

To determine n and$k$, we analyzed the ratio of the Fourier transform of received signals, and using (3), and (5), we obtained

$$\frac{Y_{n,k}(\omega)}{Y_{ref}(\omega)} = \frac{H_{n,k}(\omega)}{H_{ref}(\omega)}, \tag{6}$$

$$\frac{Y_{n,k}(\omega)}{Y_{ref}(\omega)} = \frac{S_{n,k,Tx}(\omega)S_{n,k,Rx}(\omega)e^{-j\omega\tau_{n,k}}e^{-\omega k\frac{d}{c_0}}}{S_{ref,Tx}(\omega)S_{ref,Rx}(\omega)e^{-j\omega\tau_{ref}}}, \tag{7}$$

because of the symmetrical sensors, we obtained

$$\frac{Y_{n,k}(\omega)}{Y_{ref}(\omega)} = \frac{S_{n,k}^2(\omega)e^{-j\omega\tau_{n,k}}e^{-\omega k\frac{d}{c_0}}}{S_{ref}^2(\omega)e^{-j\omega\tau_{ref}}}, \tag{8}$$

$$\frac{Y_{n,k}(\omega)}{Y_{ref}(\omega)} = G_{n,k,ref}(\omega).\ e^{-\omega k\frac{d}{c_0}}.e^{-j\omega(\tau_{n,k}-\tau_{ref})}, \tag{9}$$

where$G_{n,k,ref}(\omega) = \left[S_{n,k}(\omega)/S_{ref}(\omega)\right]^2$. If $S_{n,k}(\omega) = S_{ref}(\omega)$,

n can be obtained from the phase of $Y_{n,k}(\omega)/Y_{ref}(\omega)$ and k can be obtained from the magnitude, which is a conventional method that can be used if the sensors are not submerged in the medium [4]. In our case we could not a priori assume that $S_{n,k}(\omega) \neq S_{ref}(\omega)$, since the sensors were submerged in the woodchips. We introduced an effective refractive index, $\tilde{n}_{eff} = n_{eff} + jk_{eff}$, which describes the phase and magnitude vs. ω,

$$\angle\left(Y_{n,k}(\omega)/Y_{ref}(\omega)\right) = -\omega\frac{d(n_{eff}-1)}{c_0} \tag{10}$$

$$\left|Y_{n,k}(\omega)/Y_{ref}(\omega)\right| = \exp(-\omega k_{eff}\frac{d}{c_0}) \tag{11}$$

If $S_{n,k}(\omega) = S_{ref}(\omega)$, then $G_{n,k,ref}(\omega) = 1$ and $n_{eff} = n$ and $k_{eff} = k$. From experimental data, we can determine $\tilde{n}_{eff} = n_{eff} + jk_{eff}$ by fitting straight lines to the magnitude and phase in (10) and (11) vs. ω.

To determine $\tilde{n} = n + jk$ rather than $\tilde{n}_{eff} = n_{eff} + jk_{eff}$, we performed EM simulations of the sensor design (Fig. 2) on the geometry in Fig. 1. The ANSYS software was used. The simulations were performed using the boundary condition mode. In the simulations, we simulated $Y_{ref}(\omega)$ and $Y_{n,k}(\omega)$ for n in the range 1.08 to 1.98 and $k$in the range 0.01 to 0.49, which cover the values expected for woodchips [4]. The input signal used in the simulations was also an UWB pulse similar to the experimental signal (see Fig. 7). For each $\tilde{n} = n + jk$in the simulations, we determine $\tilde{n}_{eff} = n_{eff} + jk_{eff}$ using (10) and (11) from the simulated signal $Y_{ref}(\omega)$ and$Y_{n,k}(\omega)$. Table I shows effective $\tilde{n}_{eff} = n_{eff} + jk_{eff}$ for the$\tilde{n} = n + jk$. The table is, thus, a look-up table (LUT) that can be used to determine $\tilde{n} = n + jk$ from effective$\tilde{n}_{eff} = n_{eff} + jk_{eff}$,obtained from the experimental data. The use of the LUT, thus, enables compensation of the effects of sensor coupling on the determined refractive index.

Thus, we determined $n$and k from the experimental data in two steps:

1) Determine n_{eff} and k_{eff} from the measured signals' Fourier transform using (10) and (11).

2) Use the LUT to determine $n$and k from $n_{eff}$and k_{eff} to compensate for the effect of coupling between the sensor and the medium and perform NFCC.

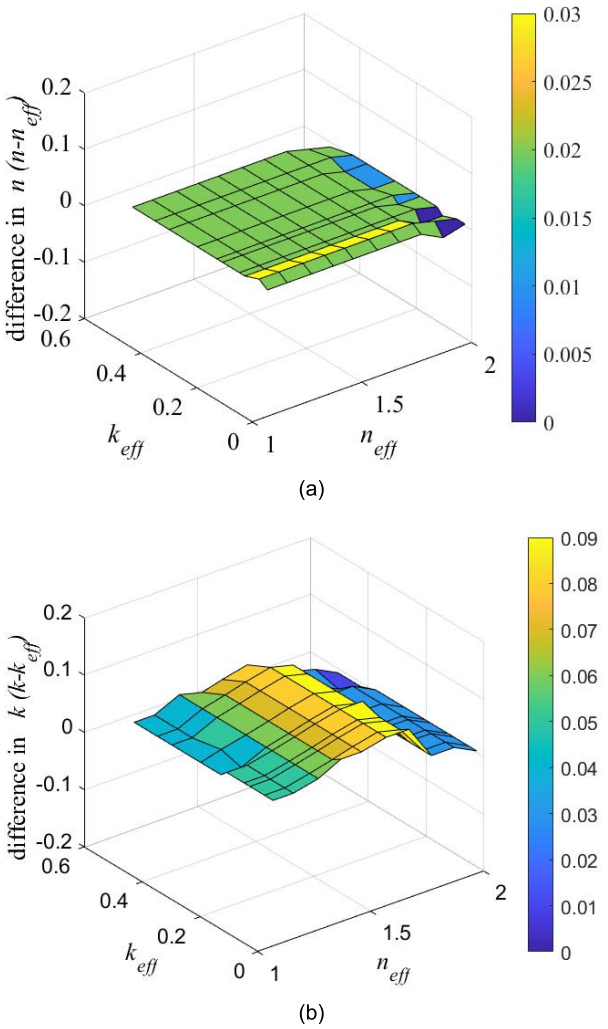

Fig. 5. The error in, (a) real part of complex refractive index, i.e., $n-n_{eff}$, and (b) imaginary part of refractive index, i.e., $k-k_{eff}$, vs. n_{eff} and k_{eff}.

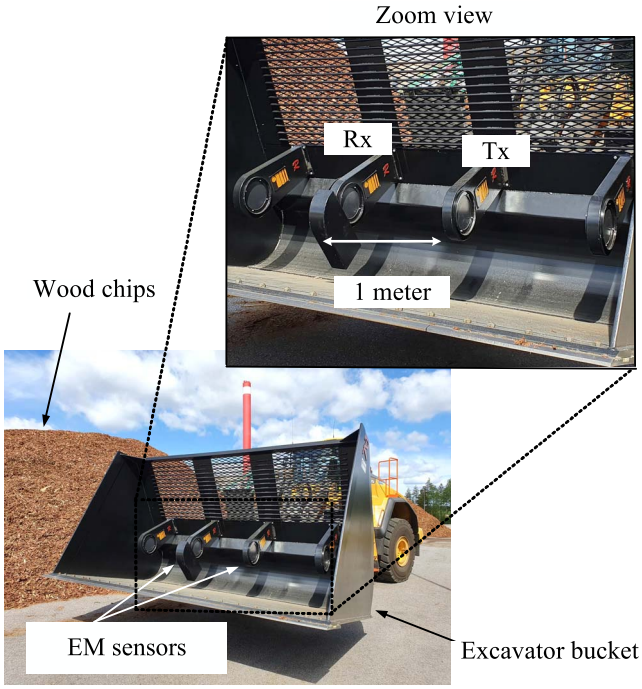

Fig. 6. Photograph of an excavator bucket and woodchips at a district heating plant. The EM sensors were attached inside the excavator bucket and arranged along the length of the bucket (see zoom view). They were used to measure woodchips' moisture content. Measurements were performed during loading or unloading of woodchips in a district heating plant.

Fig. 5 (a) shows the difference $n - n_{eff}$ vs. n_{eff} and k_{eff}. Similarly, Fig. 5(b) shows $k - k_{eff}$ vs. n_{eff} and k_{eff}. Fig. 5 illustrates the data in the Table I. If there were no effects of near-field coupling in the case of the sensors submerged in the woodchips, $n-n_{eff} = 0$ and $k-k_{eff} = 0$ for all values of n_{eff} and k_{eff}. Therefore, for $n_{eff} = 1$ and $k_{eff} = 0$, $n-n_{eff}$=0, and $k - k_{eff}$=0. Notice that $n - n_{eff}$ and $k - k_{eff}$ both depend on both n_{eff} and k_{eff}. The near-field coupling effects depend on both n and k; thus, a two-dimensional LUT is needed.

B. Industrial System Experiments

A photograph of an industrial measurement setup at the district heating plant in Gävle, Sweden shown in Fig. 6. The bucket of the wheel loader was equipped with four EM sensors, where each was equipped with a woodchip collector (see second sensor from the left in Fig. 6). The collectors were used to acquire reference samples of the woodchips near the sensors during the test period. The bucket was used to transport woodchips stored in outdoor piles into the tipping pocket, after which the woodchips were blended for 24 h in a silo and thereafter transported on a conveyor band to the furnace of a district heating plant. Woodchips can also be transported to a pulp or a paper mill. Due to the shape of the storage piles, there may be a large spread of the moisture content in the woodchips. In autumn and wintertime, the pile's surface will be moister, while the interior will be dryer. The opposite occurs during dryer seasons. The bottom of the pile is also moister. Consequently, there can be a large mix of moisture content in the bucket. Four sensors give three 1-meter measurement zones with three direct radio links. These zones give an average representation of the refractive index in the bucket. Nevertheless, reference measurements with the collectors were not an exact representation of the woodchips between the sensors. Therefore, measurements have also been performed by taking 12 samples from each bucket, so that, the measured moisture content should be comparable. Note that data from the far left and far right sensors (see zoom view of the bucket) were not included in this paper.

An example of a reference signal and a signal through woodchips are shown in Fig. 7 (a). The magnitude of the Fourier transform of both the signals after using the time windowing technique are shown in Figure 7 (b). For the reference measurement in Fig. 7 (a), we can see the delay due to propagation of EM signal through air before being received. For the measurement with woodchips, we can see the delay and attenuation clearly. In Fig.7 (b), the magnitude spectra of the signals show that the operational frequency band is 0.5–2.0 GHz. The refractive index from the bucket measurements was obtained in two ways: I) using (10), and (11) with no NFCC compensation; II) using (10), and (11) with NFCC

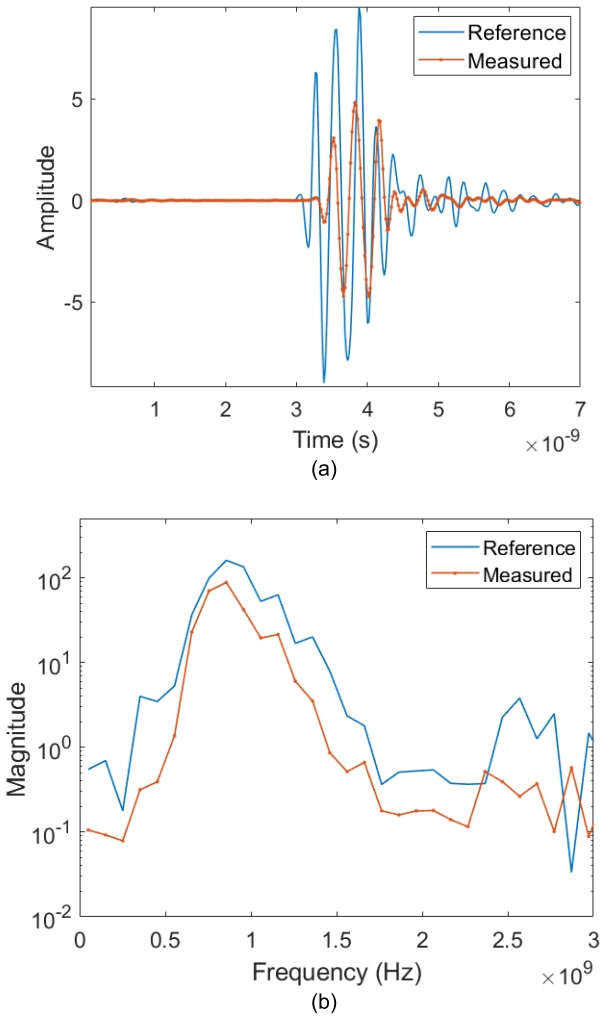

Fig. 7. A reference signal and a measured signal of the bucket measurement. (a) Measured time-domain signals, and (b) magnitude of frequency-domain signals.

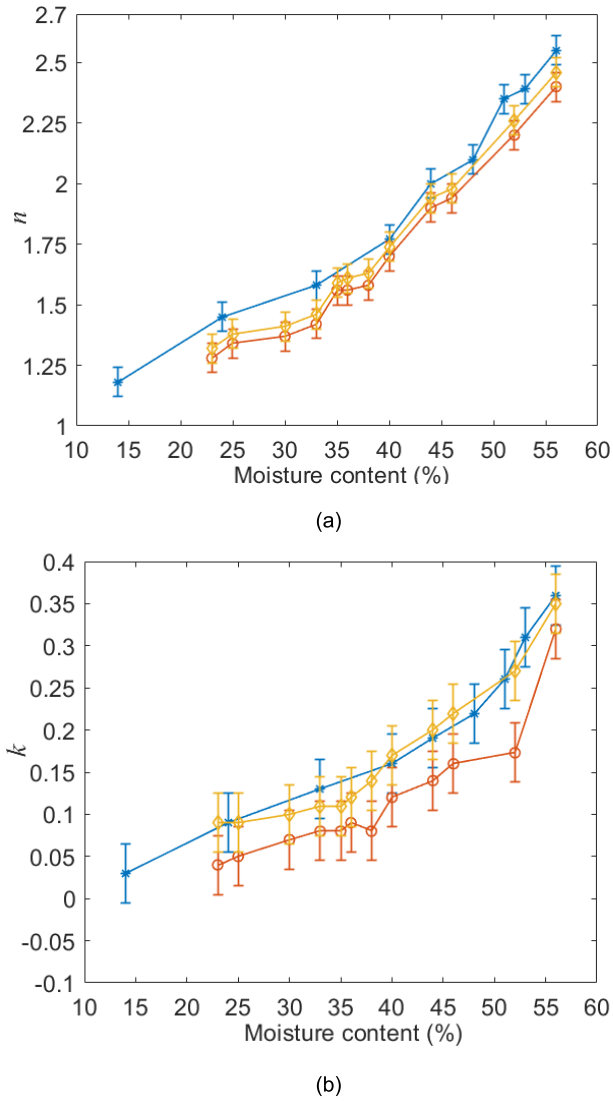

Fig. 8. Complex refractive index of woodchips vs. moisture content: (a) real part, *n*, and (b) imaginary part, *k*. Star-shaped marker (blue line) shows data from laboratory measurement (with no NFCC). Circle-shaped marker (orange line) shows industrial measurements (with no NFCC). Diamond-shaped marker (yellow line) shows industrial measurements (with NFCC).

using LUT with 2D interpolation. The experimental data are presented in Subsection C, where they are compared with data from laboratory experiments.

In the industrial application, it is preferable to determine moisture content from the measured refractive index. In the experiments, the bucket was filled with woodchips by digging into the pile. Woodchips in the bucket's collector were selected for measuring the moisture content, using the following procedure:

1) Take a sample and place it in a paper bag (sample <500 g).
2) The bag with the sample is weight (w_{wet}).
3) The bag with the sample is dried, which is carried out in a drying oven at +105 °C for 24 hours.
4) The bag with the sample is weight (w_{dry}).
5) The ratio of moist weight to dry weight gives the moisture content (wet based) [25]. The moisture content is calculated ($\mathrm{MC} = \left(w_{wet} - w_{dry}\right)/w_{wet}$).

During three field tests at Gävle Energi (i.e., a district heating plant in Sweden), 21 bucket measurements were performed. The assortment was bark of conifer trees, and predominantly spruce. Four samples were taken from the collectors (1 liter each) for all measurements. For the last seven measurements, ten additional samples were taken equivalently distributed from the whole bucket. Some of the measurements became corrupt due to incorrect filling of the bucket, which led to multi-pathing. The results are based on 12 measurements to give full coverage of the moisture contents (see Fig. 8).

C. Laboratory Experimental Verification

Measurements of the refractive index were performed at different moisture contents in the laboratory setup shown in Fig. 9, for which NFCC was not needed, since the sensors were in air outside the box. The test box was equipped with four radio sensors, which could be rotated in a horizontal and vertical direction. Besides the sensors, the test box consisted

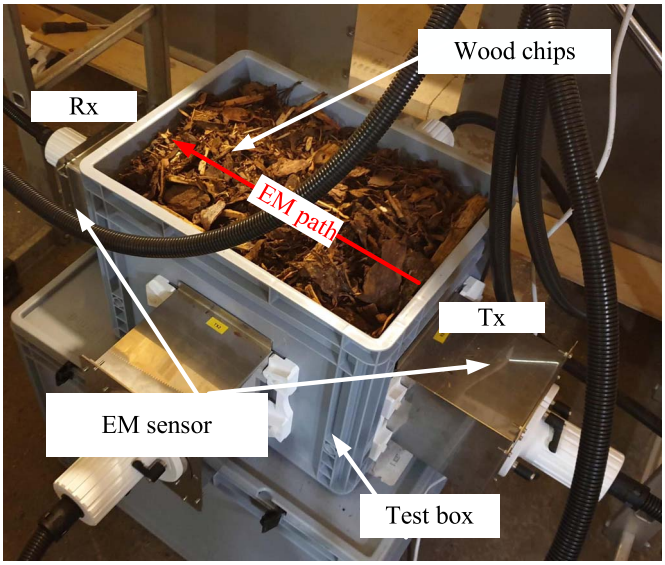

Fig. 9. Photograph of the test box measurement setup. The EM sensors housing were attached to the walls of the test box for short- and long-side measurements. Tx and Rx are the transmitting and receiving antenna, which are connected to transmitter and receiver unit of the sensing system. The distance between the antennas is 40 cm.

of a so-called eurobox with a size of 40 × 30 × 32 cm^3 (i.e., about 30 liters in volume). It is important that the woodchips in the eurobox are packed in the same way to achieve equal density between every test. Therefore, the eurobox was hit on the ground three times, refilled, hit again, and refilled. The sensors could be rotated to enable the measurement of the anisotropic properties of the woodchips [18]. The radio signal propagates faster for signals with an E-field in the vertical direction than in the horizontal direction. In this paper, measurements in the vertical direction of a long distance (40 cm) were used (see the marked EM sensors in Fig. 9) since the purpose was a comparison with the industrial measurements described above. More, in Fig. 9 the transmitting and receiving sensors are connected to transmitter and receiver unit of the sensing system as shown in the Fig.1.

The moisture content measurements were easier to define with high accuracy in the test-box than in the bucket (see Subsection B) since all woodchips can be weighted and dried. However, the test box setup was calibrated using well-known objects such as air and water (with known permittivity, $\varepsilon_{air} = 1$ and $\varepsilon_{water} = 81$).

It is time consuming to locate woodchips with varying moisture content in the piles. Therefore, the measurements in the test box were performed in a controlled manner. The same woodchips were first dried and then moistened successively by adding water and by mixing the woodchips in a cement blender. The moisture content was controlled by weighting between every adding cycle. Samples for drying were also taken for the first dried chips and after every measurement cycle. The refractive index of the verification measurements was obtained using (10) and (11), and no NFCC was used since the sensors were in air outside the test box. The results are based on nine measurements to give full coverage of the moisture contents (see Fig. 8). The assortment was bark, of the same type used in the measurements in the bucket.

In Fig. 8, n and$k$ are shown vs. moisture content from industrial and laboratory measurements. From the industrial measurements, n and$k$ were determined using NFCC as well as without NFCC. In Fig. 8(a), we can see that NFCC causes the industrial and laboratory values for n to be in agreement, although the effect is relatively small. Using NFCC, the differences are within the experimental errors. In Fig. 8(b), the difference in$k$ between the industrial and laboratory data is larger than for$n$. Additionally, NFCC causes the data from industrial and laboratory measurements to be in agreement. Thus, NFCC gives excellent agreement between industrial and laboratory measurements, well within the errors for both n and$k$; the effect is larger for k than for$n$.

D. Sensing System Characteristics

In the industrial application, it is desirable to determine the moisture content from the complex refractive index. Analytical expressions are suitable, and we used polynomials of different order. We found that second order polynomials were sufficient to model the experimental data in Fig 8. Higher polynomial orders result in over modelling. Thus, we write

$$M_n = a_0 + a_1 n + a_3 n^2, \tag{12}$$

$$M_k = b_0 + b_1 k + b_3 k^2, \tag{13}$$

where M_n and are the moisture content for the polynomials in n and k, respectively, and$a_1, a_2, \ldots, b_2$ are model polynomial coefficients. Notice that (12) and (13) are the inverse of the transfer functions from moisture content to n and k, respectively, shown in Fig. 8. Thus, the moisture content can be determined form both n and k. In order to use the information in both n and k, we calculate the moisture content as the weighted sum,

$$M = \frac{\sigma_k^2}{\sigma_n^2 + \sigma_k^2} M_n + \frac{\sigma_n^2}{\sigma_n^2 + \sigma_k^2} M_k. \tag{14}$$

Eq. (14) is the sensor fusion formula [26] of$M_n$andM_k, where σ_n and σ_k are the errors in n and k, respectively. It is assumed that the errors in n and k, i.e., σ_n andσ_k are statistically independent, which in this case is motivated by the fact that n and k are determined from the phase and amplitude (*cf.* Eq. (10) and (11)). The power spectrum of noise is typically constant, whereas the phase varies randomly between 0 and 2π.

We determined the polynomial coefficients from the laboratory data in Fig. 8 by least square fitting. The fitted lines are shown in Fig. 10 (a). Also shown are least square fitted straight lines. We describe the properties of the sensing system in terms of sensor characteristics [27]. The sensitivity is different to n and k, and we calculate it from (12) and (13) as $S_n = 1/(\partial M_n/\partial n)$ and $S_k = 1/(\partial M_k/\partial n)$ [28]. Fig. 10 (a) shows that both S_n and S_k increase with moisture content, in agreement with the increasing slope of n and k in Fig. 8.

We estimate the linearity as the maximum deviation of the transfer function and a straight line for n and k in Fig. 10 (a). The linearity in n, is 3.3 % (at moisture content = 13%)

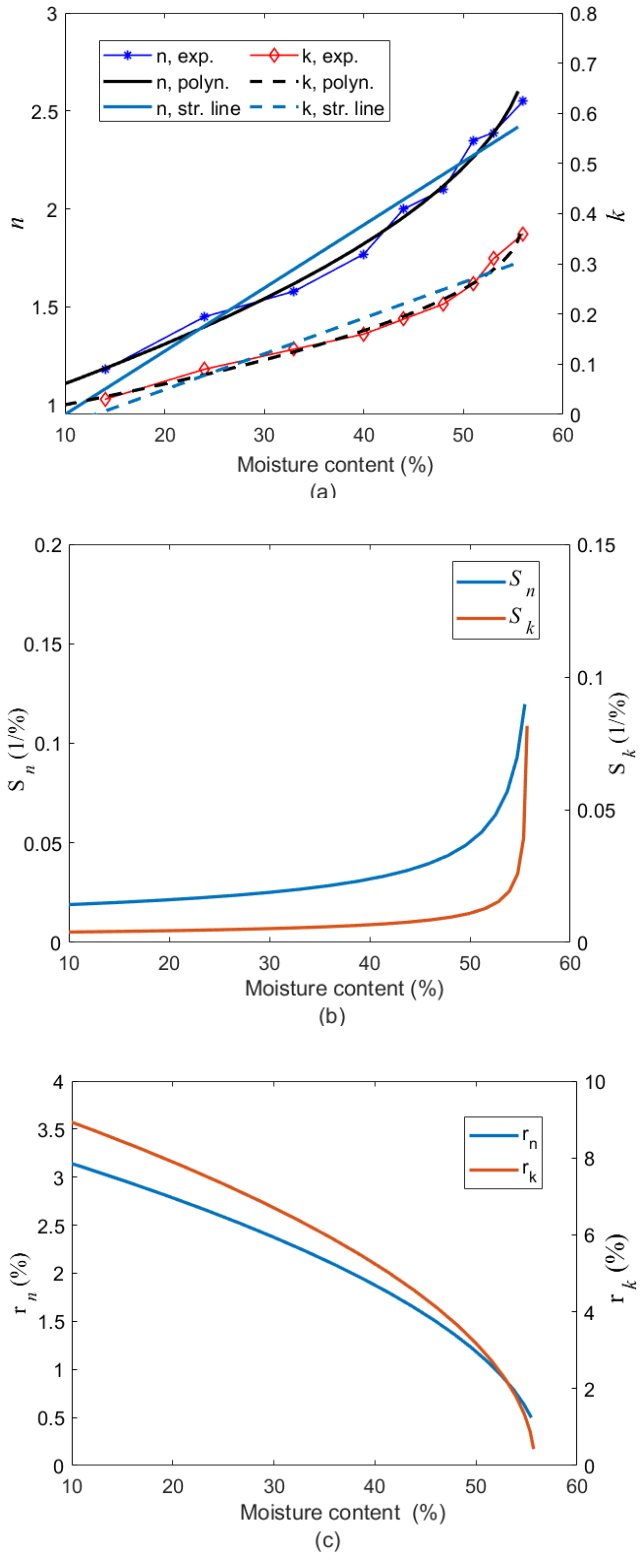

Fig. 10. (a) Fitted polynomials and straight lines, to experimental data for n and k, vs moisture content, (b) Sensitivity to n and k, (S_n and S_k, respectively) vs moisture content and (c), resolution in n and k, (r_n and r_k, respectively) vs moisture content respectively.

and in k, it is 4.0 % (at moisture content = 14%). It is clearly seen in Fig. 10 (a) that non-linear inverse functions as in Eq. (12) and (13) are needed to determine moisture content from n and k, respectively. The sensing system's range is determined by the moisture content of the calibration data, i.e., its minimum is $M_{min} = 14$ % and its maximum $M_{max} = 56$ %. The detection limit is therefore a function of the calibration data rather than the noise of the system.

The resolution in n is estimated as $r_n = \sigma_n / S_n$ and resolution in k as $r_k = \sigma_k / S_k$, [28] and is shown in Fig. 10 (c). The resolution varies with moisture content since the transfer function in n and k is nonlinear. The resolution in n is smaller than in k because of the larger error in k, as seen in Fig. 8.

We used the analytical expressions in (12), (13) and (14) to calculate the moisture content from measured n and k for both the laboratory and industrial data. In Fig. 11 (a) the calculated moisture content is shown vs the measured moisture content for the laboratory data. Thus, Fig. 11 (a) shows the error in the fitted analytical expressions (12), (13), and (14). Fig. 11 (b) shows the calculated vs measured moisture content, when n and k without NFCC was used. The calculated vs measured moisture content when n and k obtained using NFCC is shown in Fig. 11 (c).

The data points in Fig 11 (c) are closer to the straight line than those in Fig. 11 (b). The data points in Fig. 11 (b) are systematically below the straight line that indicates equality, which means that when NFCC is not used there is a systematic error in the determined moisture content.

The root mean square of the errors in Fig. 11 (a) is 1.27 percentage (pe), 1.16 pe and 1.05 pe using (12), (13), and (14), respectively. These data are measures of how well the polynomials fit the laboratory curves in Fig. 8. For Fig. 11 (b), the root mean square of the errors using (12), (13), and (14) are 4.80 pe, 8.95 pe and 7.79 pe, respectively. For the data in Fig. 11 (c), the root mean square of the errors are 3.37 pe, 2.36 pe and 2.34 pe, using (12), (13), and (14), respectively. Thus, using NFCC gives an improvement in standard deviations from above 5 pe to approximately 2 pe. The difference between the analytical expression (see (12), (13), and (14)) is relatively small, the lowest root mean square value for the industrial data is obtained by the sensor fusion formula in (14).

IV. Discussion

The presented method for NFCC could be used in other applications where EM sensors are submerged or in contact with unknown media, e.g., in geophysics, ground penetrating radar, or through the wall imaging (*cf*. Introduction). The LUT is specific for a specific sensor (or antenna) design and experimental geometry. For varying experimental geometry, the LUT must be multidimensional to include, e.g., antenna distance or antenna orientation. NFCC using a LUT could also be used in applications in which the scattering parameters (S-parameters) are measured.

The agreement between n and k from the industrial and laboratory experiments is excellent, when NFCC was used in the former case. Note that the woodchips were not the same in the two cases. In the industrial measurements, the woodchips were from an outdoor pile. In the laboratory case, the woodchips were moisturized as part of the experiment. The water distribution (on the microscopic level) may therefore have varied between the two experiments. Additionally, the

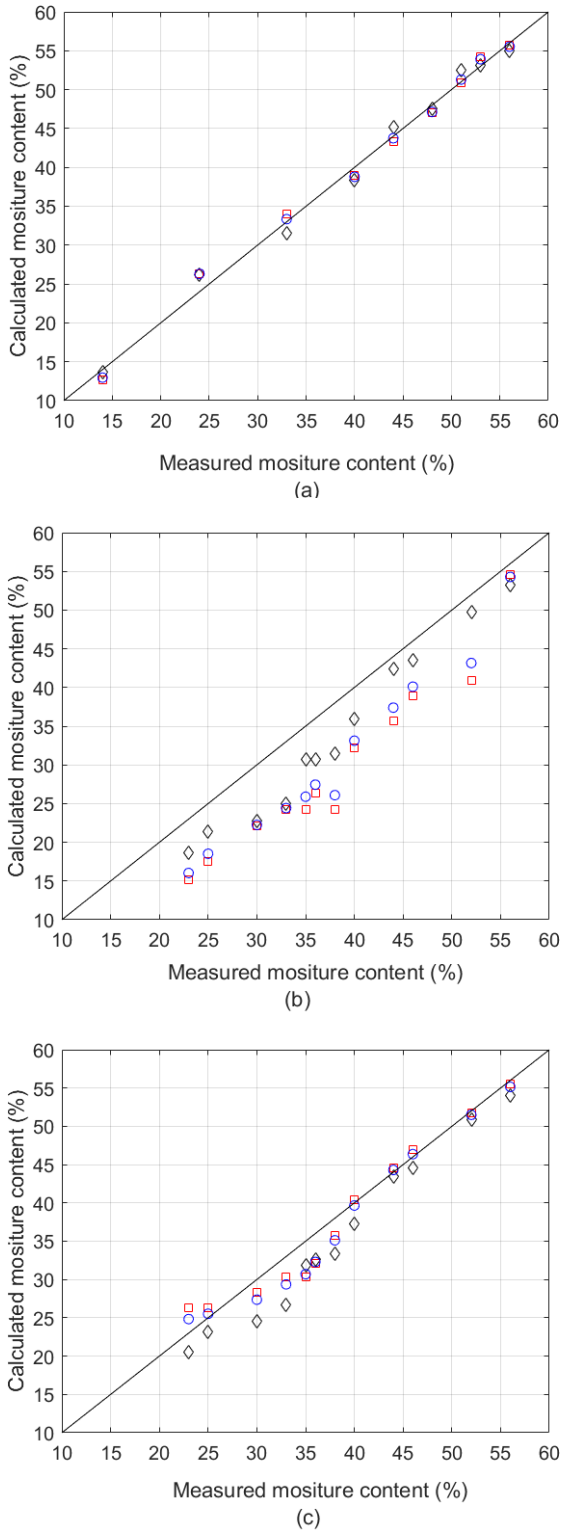

Fig. 11. Calculated vs. measured moisture content. (a) Laboratory data, (b) industrial with no NFCC, and (c) industrial with NFCC. Black diamond-shaped markers correspond to (12) (wherein n is used). Red square-shaped markers correspond to (13) (wherein k is used). Blue circle-shaped markers correspond to (14) (wherein both n and k are used). The black solid line shows the ideal case, when calculated and measured moisture content are equal.

orientation due to gravity may have been different in the two cases.

V. Conclusion

An EM sensor was designed, manufactured and characterized for the purpose of measuring the complex refractive index of woodchips (in buckets for wheel loaders) in industrial applications.

The coupling between the sensor and the woodchips makes the determination of the woodchips' n and k difficult. Conventional time or frequency domain methods cannot be used for accurate results. We thus propose a method for NFCC. EM simulations were used to obtain a two dimensional LUT, which was further used for NFCC. The LUT contained a correction that was applied to n and k as determined from a conventional frequency-domain technique.

Industrial and laboratory measurement were made in which the n and k of woodchips of different moisture contents were determined. Using the NFCC method excellent agreement was found between the industrial and laboratory measurements.

The excellent agreement between the laboratory and industrial measurements shows that laboratory measurements can be used when designing industrial nondestructive testing using radar or radio-link signals, if the proper corrections are made for different geometries.

Polynomials fitted to laboratory data were used to calculate the moisture content of woodchips in the industrial experiment from the determined n and k. A standard deviation of approximately 2 pe was achieved using NFCC, as compared to more than 5 pe without NFCC.

Acknowledgment

The authors would like to thank other team members at Radarbolaget AB for software and technical support.

References

[1] C. Le, T. Dogaru, L. Nguyen, and M. A. Ressler, "Ultrawideband (UWB) radar imaging of building interior: Measurements and predictions," *IEEE Trans. Geosci. Remote Sens.*, vol. 47, no. 5, pp. 1409–1420, May 2009.

[2] M. Džunda, P. Dzurovčin, P. Kalavský, P. Korba, Z. Cséfalvay, and M. Hovanec, "The UWB radar application in the aviation security systems," *Appl. Sci.*, vol. 11, no. 10, p. 4556, May 2021.

[3] J. Liang and F. Zhu, "Soil moisture retrieval from UWB sensor data by leveraging fuzzy logic," *IEEE Access*, vol. 24, pp. 29846–29857, 2018.

[4] V. Choudhary and D. Rönnow, "A nondestructive testing method for the determination of the complex refractive index using ultra wideband radar in industrial applications," *Sensors*, vol. 20, no. 11, p. 3161, Jun. 2020.

[5] R. B. McIntosh and M. E. Casada, "Fringing field capacitance sensor for measuring the moisture content of agricultural commodities," *IEEE Sensors J.*, vol. 8, no. 3, pp. 240–247, Mar. 2008.

[6] J. Pietilä, A. Yli-Korpela, E. Ikonen, and O. Timonen, "Monitoring and control of chip quality in chemical pulping," *Nordic Pulp Paper Res. J.*, vol. 30, no. 1, pp. 149–159, Jan. 2015.

[7] D. Černý, J. Malaták, and J. Bradna, "Influence of biofuel moisture content on combustion and emission characteristics of stove," *Agronomy Res.*, vol. 14, no. 3, pp. 725–732, 2016.

[8] C. Schön, D. Kuptz, R. Mack, V. Zelinski, A. Loewen, and H. Hartmann, "Influence of wood chip quality on emission behaviour in small-scale wood chip boilers," *Biomass Convers. Biorefinery*, vol. 9, no. 1, pp. 71–82, Mar. 2019.

[9] E. Oveisi *et al.*, "Characterization of recycled wood chips, syngas yield, and tar formation in an industrial updraft gasifier," *Environments*, vol. 5, no. 7, p. 84, 2018.

[10] B. Guan, A. Ihamouten, X. Dérobert, D. Guilbert, S. Lambot, and G. Villain, "Near-field full-waveform inversion of ground-penetrating radar data to monitor the water front in limestone," *IEEE J. Sel. Topics Appl. Earth Observ. Remote Sens.*, vol. 10, no. 10, pp. 4328–4336, Oct. 2017.

[11] K. K.-M. Chan, A. E.-C. Tan, L. Li, and K. Rambabu, "Material characterization of arbitrarily shaped dielectrics based on reflected pulse characteristics," *IEEE Trans. Microw. Theory Techn.*, vol. 63, no. 5, pp. 1700–1709, May 2015.

[12] D. Oloumi, K. K.-M. Chan, P. Boulanger, and K. Rambabu, "SAGD process monitoring in heavy oil reservoir using UWB radar techniques," *IEEE Trans. Microw. Theory Techn.*, vol. 64, no. 6, pp. 1884–1895, Jun. 2016.

[13] K. Teng *et al.*, "Embedded smart antenna for non-destructive testing and evaluation (NDT&E) of moisture content and deterioration in concrete," *Sensors*, vol. 19, no. 3, p. 547, Jan. 2019.

[14] H. Zemmour, G. Baudoin, and A. Diet, "Effect of depth and soil moisture on buried ultra-wideband antenna," *Electron. Lett.*, vol. 52, no. 10, pp. 792–794, 2016.

[15] J. Avva, J. M. Kovac, C. Miki, D. Saltzberg, and A. G. Vieregg, "An *in situ* measurement of the radio-frequency attenuation in ice at summit station, Greenland," *J. Glaciol.*, vol. 61, no. 229, pp. 1005–1011, 2015.

[16] A. S. Kesar and E. Weiss, "Wave propagation between buried antennas," *IEEE Trans. Antennas Propag.*, vol. 61, no. 12, pp. 6152–6156, Nov. 2013.

[17] V. Choudhary, "Nondestructive testing and antenna measurements using UWB radar in industrial applications," Ph.D. dissertation, Tech. Inf. Sci., KTH Roy. Inst. Tech., Stockholm, Sweden, 2021.

[18] P. Ottoson, D. Andersson, and D. Rönnow, "UWB radio measurement and time-domain analysis of anisotropy in wood chips," *IEEE Sensors J.*, vol. 18, no. 22, pp. 9112–9119, Nov. 2018.

[19] Y. Yang, Y. Wang, and A. E. Fathy, "Design of compact Vivaldi antenna arrays for UWB see through wall applications," *Prog. Electromagn. Res.*, vol. 82, pp. 401–418, 2008.

[20] N. Telzhensky and Y. Leviatan, "Planar differential elliptical UWB antenna optimization," *IEEE Trans. Antennas Propag.*, vol. 54, no. 11, pp. 3400–3406, Nov. 2006.

[21] (2021). *Ansys Electronics, Complete Electronics Simulation Tools*. Accessed: Oct. 11, 2021. [Online]. Available: https://www.ansys.com/products/electronics

[22] D. M. Pozar, *Microwave Engineering*, 4th ed. Hoboken, NJ, USA: Wiley, 2012, p. 690.

[23] G. A. Niklasson, "Modeling the optical properties of nanoparticles," *SPIE Newsroom*, vol. 10, p. 182, Oct. 2006.

[24] B. R. Mahafza, "Near and far field regions," in *The Introduction to Radar Analysis*. New York, NY, USA: CRC Press, 2017, p. 343.

[25] S. V. Glass and S. L. Zelinka, "Moisture relations and physical properties of wood," Wood Handbook -Wood Eng. Mater., Forest Products Lab. Gen. Dept. Agricult., Forest Service, Forest Products Lab., Madison, WI, USA Tech. Rep. FPL-GTR-190, 2010.

[26] F. Gustafsson, *Statistical Sensor Fusion, Student Literature*. Lund, Sweden: Studentlitteratur, 2012, ch. 2.

[27] J. Fraden, "Sensor characteristics," in *Handbook of Modern Sensors, Physics, Design, and Application*, 4th ed. New York, NY, USA: Springer, 2010.

[28] A. D'Amico and C. Di Natale, "A contribution on some basic definitions of sensors properties," *IEEE Sensors J.*, vol. 1, no. 3, pp. 183–190, Oct. 2001.

Vipin Choudhary (Member, IEEE) received the Master of Technology degree in wireless communication, electronics from Amity University, Uttar Pradesh, in 2017, and the Licentiate degree in electrical engineering from the KTH Royal Institute of Technology, Stockholm, Sweden, in 2021. He is currently pursuing the Ph.D. degree in electrical engineering with collaboration of the KTH Royal Institute of Technology and the University of Gävle, Gävle, Sweden, with a focus on RF and antenna measurements, non-destructive testing, radar measurements, radar imaging, microwave/radar absorbers materials, SAR as well as polarimetry measurements, RF measurement techniques, and signal processing.

Patrik Ottosson received the M.Sc. degree in photogrammetry and geodesy and the Ph.D. degree in geo-informatics from the KTH Royal Institute of Technology, Stockholm, Sweden, in 1991 and 2001, respectively. He is currently a Managing Director at Radarbolaget, Gävle, Sweden, it develops ultra-wide band radar and radio measurement system and new technological solutions for moist wood measurement at district heating plants and at pulp plants, calcination measurement in lime shaft furnaces, and high-accuracy radar system for steel expansion measurements in heating furnaces.

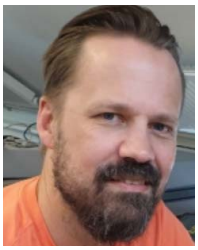

Daniel Andersson received the B.Sc. degree in electronics from the University College of Gävle, Gävle, Sweden, in 2000.

He is currently a Developer of Radar Systems and Radar Solutions with Radarbolaget, Gävle. He is the inventor of the highly accurate ultra-wide band radar and radio measurement system used for this paper.

Daniel Rönnow (Member, IEEE) received the M.Sc. degree in engineering physics and the Ph.D. degree in solid state physics from Uppsala University, Uppsala, Sweden, in 1991 and 1996, respectively.

He was with the Max Planck Institute, Stuttgart, Germany, from 1996 to 1998, and with Acreo AB, Stockholm, Sweden, from 1998 to 2000. From 2000 to 2004, he was with Racomna AB, Uppsala. From 2004 to 2006, he was a University Lecturer with the University of Gävle, Gävle, Sweden, where he became a Professor of Electronics in 2011. From 2006 to 2011, he was a Senior Sensor Engineer with WesternGeco, Oslo, Norway. He has been an Associate Professor with Uppsala University since 2000. He has authored or coauthored over 70 peer-reviewed papers. He holds eight patents. His current research interest is RF measurement techniques.